nanomanufacturing

MDPI

Article

rPET Nanofiber Membranes for Air Filtration: High Performance via Electrospinning Optimization

Gabriela Brunosi Medeiros [1,*], Paulo Augusto Marques Chagas [1], Gustavo Cardoso da Mata [1,*], Daniela Patrícia Freire Bonfim [1], Daniela Sanches de Almeida [2] and Mônica Lopes Aguiar [1]

[1] Departamento de Engenharia Química, Federal University of São Carlos, Rodovia Washington Luiz, km 235—SP 310, São Carlos 13565-905, SP, Brazil; paulochagas@ufscar.br (P.A.M.C.); daniela.bonfim@ctnano.org (D.P.F.B.); mlaguiar@ufscar.br (M.L.A.)

[2] Departamento de Engenharia Ambiental, Federal University of Technology—Paraná, Avenida dos Pioneiros, 3131, Londrina 86030-370, PR, Brazil; danielaalmeida@uttpr.edu.br

* Correspondence: gabrielamedeiros@ufscar.br (G.B.M.); gugs_cardoso@ufsj.edu.br (G.C.d.M.)

Abstract

Although recycled poly(ethylene terephthalate) (rPET) is an attractive, sustainable feedstock for electrospinning, optimization of processing variables for filtration performance remains limited. This study quantifies how polymer concentration, flow rate, and applied voltage govern fiber morphology and key filtration metrics—collection efficiency (η), pressure drop (ΔP), quality factor (Q_f), and porosity—in rPET membranes. A fractional factorial design was employed to model interactions and identify trade-offs in filtration performance. The optimal condition was obtained at 16 wt.% PET, 1.2 mL·h^{-1}, and 22 kV, yielding uniform fibers with an average diameter of 328.6 nm and high filtration efficiencies (95.65–99.99%). The permeability constants were 1.07 × 10^{-12} m^2 (20 wt.% PET) and 1.15 × 10^{-13} m^2 (8 wt.% PET), indicating an increase in permeability with increasing polymer concentration and fiber diameter. The 20 wt.% PET membrane delivered the highest Q_f of 0.0646 Pa^{-1} with a low ΔP of 48.5 Pa at 4.8 cm·s^{-1}, reflecting a favorable balance between collection and airflow resistance. In summary, higher PET concentrations reduce flow resistance and improve Q_f, whereas lower concentrations yield finer fibers and high η at the expense of permeability. rPET nanofiber membranes, therefore, represent a sustainable and versatile route to high-efficiency, lower-pressure-drop air filters for residential, industrial, and commercial environments.

Keywords: electrospinning; recycled PET; nanofibers; air filtration; factorial design

Check for updates

Academic Editor: Candido Fabrizio Pirri

Received: 10 October 2025
Revised: 14 November 2025
Accepted: 3 February 2026
Published: 5 February 2026

Copyright: © 2026 by the authors. Licensee MDPI, Basel, Switzerland. This article is an open access article distributed under the terms and conditions of the Creative Commons Attribution (CC BY) license.

1. Introduction

Rapid urbanization and industrial activity have intensified global concerns regarding air pollution and its impacts on human health and environmental sustainability. Ambient airborne pollutants—particularly fine and ultrafine particulate matter (PM)—are associated with respiratory and cardiovascular disease and increased mortality [1,2]. By infiltrating organ tissues, these particles trigger oxidative stress, inflammatory responses, and apoptosis [3]. The ultrafine fraction (PM0.1) is especially harmful, exhibiting greater toxicity than PM2.5 [4]. According to the World Health Organization, 99% of the global population breathes air with pollutant levels above recommended limits, underscoring the urgent need for advanced air-filtration technologies [5].

Conventional filtration systems, such as High-Efficiency Particulate Air (HEPA) filters, are effective for removing fine particles; however, their relatively high pressure drops at

typical face velocities increase energy consumption and operating costs. Furthermore, their reliance on single-use, hard-to-recycle media poses additional sustainability challenges. These limitations highlight the need for filtration membranes that combine high collection efficiency and low flow resistance while maintaining cost-effectiveness and credible sustainability attributes [6–8].

Electrospun nanofibers have emerged as promising candidates for advanced air-filtration applications due to their interconnected pore networks, low basis weight, high surface area, and tunable morphology [9–11]. These characteristics enhance the capture of nanometric particles (<100 nm), for which Brownian diffusion and electrostatic attraction dominate over impaction and interception-based mechanisms [12–14]. Beyond filtration, electrospun nanofibers have demonstrated versatility in energy storage devices [15], sensors [16,17], catalysis [18], wound care [19,20], and clean-energy membrane systems [21], highlighting the broad applicability of this fabrication method.

Electrospinning nanofiber production is governed by three sets of variables: (i) solution properties—conductivity, surface tension, polymer concentration, viscosity, molecular weight, and dielectric constant [22]; (ii) processing conditions—applied voltage, tip-to-collector distance, and collector geometry; and (iii) environmental factors—temperature, humidity, and airflow [23]. Together, these variables regulate jet stability, charge transport, and solvent evaporation, thereby setting fiber morphology and diameter distribution—from uniform or porous fibers to bead-containing ("beads-on-a-string") structures.

A wide range of polymers can be applied to air-filtration membranes, including polyester, polypropylene, polycarbonate, and polyacrylonitrile [24]. For instance, Lima et al. [25] employed an ultra-fast (5 min) electrospinning of recycled polystyrene (PS) using DL-limonene to produce nanofiber membranes that capture 99.97% of nanometric particles at low pressure drops. Silva et al. [26] fabricated electrospun polyacrylonitrile (PAN) filters doped with surfactants (CTAB, SDS, CPC), capturing over 99% of sub-250 nm aerosols at 111–204 Pa pressure drops. These filters also exhibited strong biocidal activity, inactivating *Staphylococcus aureus* (97.25 $\pm$ 0.95%) and *Escherichia coli* (94.52 $\pm$ 2.37%), yielding bifunctional filtration and antimicrobial action suited to sterile-air settings.

In this context, recycled poly(ethylene terephthalate) (rPET) emerges as a promising candidate material for air-filtration membranes due to its availability, mechanical strength, and recyclability [27]. With billions of PET bottles discarded annually, their reuse in electrospun membranes offers a sustainable and cost-effective alternative to virgin materials, addressing both environmental and economic concerns [27,28]. Prior studies have demonstrated the feasibility of electrospinning recycled PET for air filtration applications, reporting promising results in terms of filtration efficiency and permeability [29–31]. Šišková et al. [28] developed PET nanofibers for facial masks with 98% filtration efficiency, though breathability was insufficient. Strain et al. [29] optimized PET fiber diameters for smoke filtration, with 0.4 μm fibers being the most effective. Du et al. [30] produced PET nanofibers supported on PET with 87% PM2.5 filtration efficiency and superhydrophobicity. Aydemir and Demiryürek [31] identified polymer concentration as the key parameter influencing fiber diameter, while Bonfim et al. [32,33] demonstrated that reducing fiber diameter improved both filtration efficiency (up to 99%) and mechanical resistance, making PET filters suitable for various industrial and medical applications.

Recent studies have further advanced this field by incorporating recycled PET into multifunctional nanofibrous membranes. Kijeńska-Gawrońska et al. [34] developed electrospun mats from virgin and recycled PET enriched with silver nanoparticles (50–400 nm), achieving >99% filtration efficiency for particles > 1 μm and antibacterial activity against *Staphylococcus epidermidis* with 66–86% bacterial growth reduction. Similarly, Hossain et al. [35] fabricated nanofibrous membranes from recycled PET bottles with uniform fibers

(average diameter 198.5 nm), tensile strength of 20 N, and air permeability of 8.59 L·min^{-1}, achieving 97.04% filtration efficiency for 0.3 μm particles.

Despite these advances, there is still a lack of systematic optimization linking electrospinning parameters to fiber morphology and filtration performance in rPET membranes. Statistical design of experiments (DoE) has been applied to optimize poly(ethylene oxide) (PEO) nanofibers [36] and to evaluate the air-filtration performance of poly(vinyl alcohol) (PVA) and chitosan nanofibers [37,38]. This study employs a factorial design to optimize the electrospinning of recycled poly(ethylene terephthalate), modulating polymer concentration, flow rate, and applied voltage to precisely control fiber morphology and, consequently, collection efficiency and pressure drop. The factorial framework enables a comprehensive analysis of main effects and interactions, elucidates the process–structure–performance relationships, and yields membranes with tunable filtration profiles for applications ranging from residential air purification to industrial environments [39–41]. By coupling sustainable materials with statistically guided manufacturing, we demonstrate high-performance, versatile rPET membranes and contribute to next-generation air-filtration technologies for industrial, commercial, and residential use.

2. Materials and Methods

2.1. Materials

Recycled poly(ethylene terephthalate) (PET) obtained from transparent PET bottles was employed. The solvents used in the formulation of the solutions were trifluoroacetic acid (TFA; Neon Comercial Ltda., Suzano, Brazil) and dichloromethane (DCM; Labsynth Ltda., Diadema, Brazil). The electrospinning setup used 10 mL plastic syringes connected to stainless-steel needles with an inner diameter of 0.7 mm.

2.2. Preparation of the Solution and Electrospinning

Polymer solutions of PET (8–20 wt.%) were prepared in trifluoroacetic acid/dichloromethane (TFA/DCM, 70/30, *v*/*v*) [27]. Electrospinning was performed on a setup comprising a high-voltage power supply (HSensor, Maringá, Brazil), a flat aluminum plate collector, a metallic needle as the spinneret, and a syringe pump (HSensor, Maringá, Brazil) to control the flow rate. For 8, 10, and 12 wt.% PET, the operating parameters were 0.6 mL·h^{-1} (flow), 16 kV (applied voltage), and 8 cm (tip-to-collector distance). For 14, 16, 18, and 20 wt.% PET, the parameters were 1.2 mL·h^{-1}, 22 kV, and 12 cm. These conditions were selected to minimize fiber diameter based on preliminary trials and prior studies [28,30,32], which indicated that lower concentrations require lower voltage and shorter distances to achieve stable jet formation and continuous fibers, while higher concentrations demand higher voltage and longer distances to promote adequate stretching and solvent evaporation, minimizing bead formation and ensuring uniform fiber morphology. Producing uniform and bead-free fibers is particularly important for air filtration applications, where consistent pore structure and interconnected porosity strongly influence pressure drop and capture efficiency [39].

A 2^3 fractional factorial design was used to evaluate the effects of solution concentration, applied voltage, and flow rate on the average fiber diameter. Each factor was studied at two levels with center points, as summarized in Table 1. The variables selected for the factorial design (PET concentration, applied voltage, and flow rate) were chosen because they are the primary electrospinning parameters known to directly influence the jet stability, solvent evaporation, and stretching of the polymer jet during fiber formation. These factors have been consistently reported in the literature as the main parameters controlling fiber diameter, bead formation, and overall morphology in PET electrospinning systems [28,30,32]. The three concentration levels (16, 18, and 20% PET) were selected based on preliminary

trials and previously published studies, which indicated that this concentration range produces stable jets and continuous fibers without bead formation. Concentrations below 14% resulted in discontinuous jets and fibers with beads, while concentrations above 20% led to excessively high viscosity, clogging, and difficulty maintaining stable flow. Therefore, the 16–20% range represented the optimal window for obtaining thinner nanofibers suitable for filtration applications.

Table 1. A 2^3 factorial design for the study of solution and process variables.

Variable	Levels		
	Bottom	**Central**	**Top**
PET Concentration (%) (*m*/*v*)	16	18	20
Applied Voltage (kV)	16	19	22
Flow Rate (mL·h^{-1})	0.6	0.9	1.2

Similarly, the voltage and flow rate levels were selected because they corresponded to the stable electrospinning operating ranges previously identified for PET under the solvent system used (TFA/DCM). Lower voltages and flow rates were insufficient to stretch the jet at higher concentrations, whereas excessively high values led to splashing and non-uniform fibers. The tip-to-collector distance was maintained at 12 cm, which was determined from preliminary trials (8–15 cm) as the optimal spacing to minimize clogging and prevent jet spraying.

The chosen levels allowed meaningful evaluation of how these processing variables influence fiber diameter within a stable electrospinning regime. The primary response was the average fiber diameter, a parameter directly linked to filtration efficiency and permeability in nanofiber media [39]. Diameter data were analyzed using Design-Expert® v7.0.0.

2.3. Characterization of Filter Media

The nanofiber membranes were characterized by scanning electron microscopy (SEM; Philips XL-30 FEG, Eindhoven, The Netherlands). Fiber diameters were measured from SEM micrographs using ImageJ 1.53e, following the procedure described by Bortolassi et al. [42]. The average diameter and standard deviation were calculated for each sample.

The viscosity of PET solutions at different concentrations was measured at room temperature using a Brookfield LV DV-II+ viscometer (AMETEK Brookfield, Middleboro, MA, USA) equipped with an SC4-18 spindle (sample volume: 1 mL). The functional groups of the electrospun fibers were characterized by Fourier-transform infrared spectroscopy (FTIR; IRSpirit with QATR-S, Shimadzu, Kyoto, Japan).

Thermal properties were evaluated by differential scanning calorimetry (DSC; Jade DSC, PerkinElmer, Waltham, MA, USA) and thermogravimetric analysis (TGA; TGA 4000, PerkinElmer, Waltham, MA, USA). For DSC, 2–4 mg of each sample were heated from 25 to 300 °C at 10 °C·min^{-1} under a nitrogen flow of 30 mL·min^{-1}. For TGA, approximately 10 mg of each sample was heated from 25 to 800 °C at 20 °C·min^{-1} under a nitrogen flow of 20 mL·min^{-1}.

2.4. Air Filtration Properties

Permeability and aerosol filtration efficiency were measured using the setup shown in Figure 1. The system comprised an air compressor (Shulz, Joinville, Brazil), an air-purification train (model 3074B, TSI Incorporated, Shoreview, MN, USA), a particle generator (model 3079A, TSI Incorporated, Shoreview, MN, USA) with diffusion dryer (model 3062, TSI Incorporated, Shoreview, MN, USA), a bipolar radioactive neutralizer (Kr-85/Am-241; model 3054, TSI Incorporated, Shoreview, MN, USA), a filter holder, and a flow meter

(GFM17, Aalborg Instruments, Orangeburg, NY, USA). Size-resolved efficiencies were obtained with a Scanning Mobility Particle Sizer (SMPS) consisting of an electrostatic classifier (model 3080, TSI Incorporated, Shoreview, MN, USA) and a differential mobility analyzer column (DMA) coupled to an ultrafine condensation particle counter (model 3776, TSI Incorporated, Shoreview, MN, USA) [43]. In this setup, compressed air was purified through the air-purification train and partially directed to the particle generator, where a sodium chloride (NaCl) solution (0.1 $g \cdot L^{-1}$) was atomized to produce a polydisperse aerosol containing nanoparticles ranging from 6.4 to 232.9 nm (average diameter ≈ 63.5 nm). The generated droplets were dried in a diffusion dryer, forming solid NaCl particles that were subsequently charge-neutralized by a bipolar radioactive source. The resulting aerosol stream passed through the filter holder, and particle concentrations were measured upstream and downstream using the SMPS system.

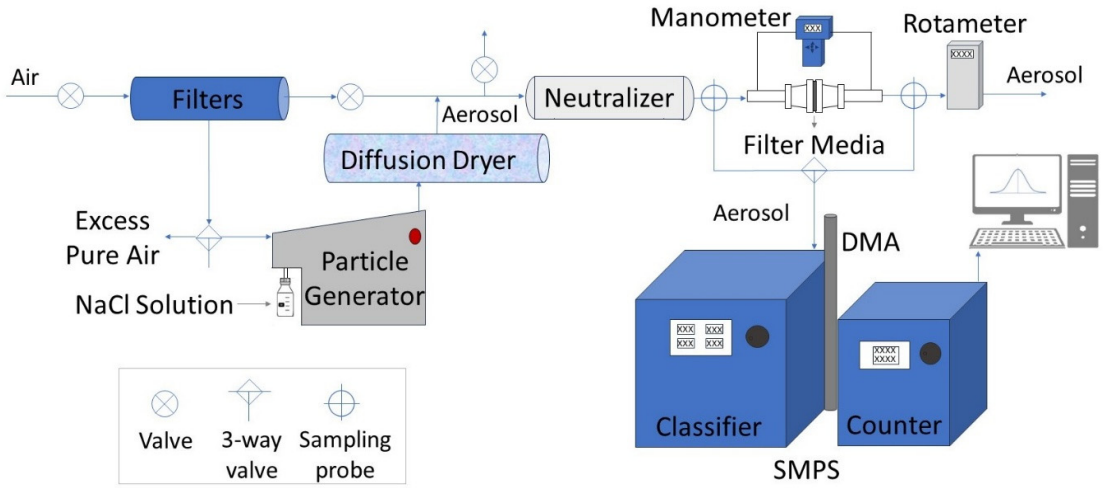


Figure 1. Schematic of the module used to determine the permeability and collection efficiency of the filter media. Arrows indicate the airflow direction, and the symbols represent valves and sampling probes.

Permeability was determined by flowing clean air (without particles) through the setup shown in Figure 1. Clean air was flowed through the filter holder at superficial velocities between 0.76 and 6.52 $cm \cdot s^{-1}$ (effective filtration area: 5.2 cm^2), and the pressure drop (ΔP) was measured using a digital manometer (VelociCalc 9555-P, TSI Incorporated, Shoreview, MN, USA). The intrinsic permeability (k_1) was then calculated from Darcy's law (Equation (1)), assuming constant thickness (L) [43].

$$\frac{\Delta P}{L} = \frac{\mu}{k_1} \times v_s \quad (1)$$

where ΔP is the pressure drop; L is the thickness of the filter media; μ is the viscosity of air (1.74×10^{-5} Pa·s); and v_s is the superficial gas velocity. The filter media thicknesses were measured using a high-precision digital thickness gauge (130.404 Digimess, Digimess Instrumentos de Precisão Ltda., São Paulo, Brazil).

Collection efficiency (η) was measured by an electrical-mobility-based method, comparing upstream and downstream particle number concentrations across the filter media (Equation (2)) [43], at a fixed face (superficial) velocity of 4.8 $cm \cdot s^{-1}$ over a 5.2 cm^2 effective area.

$$\eta = \frac{C_i - C_f}{C_i} \quad (2)$$

where C_i is the concentration of particulate material at the inlet of the filter media, and C_f is the concentration of particles at the outlet of the filter media.

As previously mentioned, the major challenge in air filter production is the search for and development of efficient filter media that minimize pressure drop. Based on this, the quality factor (Q_f) was calculated (Equation (3)), which relates the pressure drop (ΔP) to the particle removal efficiency (η) [44].

$$Q_f = \frac{-ln(1-\eta)}{\Delta P} \tag{3}$$

Theoretical porosity (φ_{teo}) was estimated to quantify the void fraction between fibers using the Davies (1953) relation (Equation (4)), which has been applied to experimental datasets of nanofiber and microfiber media [45].

$$\frac{\Delta P}{L} = v_s \times \frac{\mu}{r^2} \times 16 \times (1-\varphi_{teo})^{1.5} \times \left(1 + 56 \times (1-\varphi_{teo})^3\right) \tag{4}$$

where r is the fiber radius, taken as the average radius measured from SEM images. As in the permeability analysis, we used the linear relation between $\Delta P/L$ versus v_s to compute φ for each sample.

In addition to theoretical porosity, experimental porosity was determined as the ratio of void volume to total volume. Samples were cut into 1 × 1 cm squares, weighed, and their thickness measured. Two methods were used. The first followed Equation (5) [46], where m is the sample mass, v its volume (thickness × area), and ρ_{PET} the PET density (1.38 g·cm^{-3}).

$$\varphi_{exp} = 1 - \frac{m}{\rho_{PET} \times v} \tag{5}$$

The second method was butyl alcohol uptake: samples were immersed in butyl alcohol for 1 h, and experimental porosity was then calculated using Equation (6) [47].

$$\varphi_{exp} = \frac{m_{BuOH}/\rho_{BuOH}}{(m_{BuOH}/\rho_{BuOH}) + (m_s/\rho_{PET})} \tag{6}$$

where m_{BuOH} is the mass of butyl alcohol absorbed, m_s is the dry sample mass, and ρ_{BuOH} and ρ_{PET} are the densities of butyl alcohol (0.81 g·cm^{-3}) and PET, respectively.

3. Results

3.1. Statistical Analysis

The statistical analysis was conducted to qualitatively assess the effects of each parameter on the fiber diameter. The contribution of each parameter and the interaction among them on the response (average diameter) was estimated using Pareto's diagram, obtained through the Design-Expert® v7.0.0 software, and the results are presented in Table 2. This contribution is given as a percentage.

Table 2. Percentage of contribution of the variables studied according to Pareto's diagram.

Variable	Contribution (%)
Applied voltage	30.33
PET concentration	19.01
PET concentration/applied voltage	11.14
PET concentration/flow rate	3.32
Flow rate	0.17
Flow rate/applied voltage	0.05
PET concentration/flow rate/applied voltage	0.01
Curvature	35.24
Pure error	0.73

The Pareto analysis (Table 2) indicates that the applied voltage was the dominant parameter influencing the fiber diameter, followed by PET concentration, while the flow rate had a negligible main effect. Increasing the applied voltage from 16 to 22 kV reduced the average diameter from 518 to 363 nm ($\Delta \approx -155$ nm), with a stronger drop at higher PET (-249 nm at 20% vs. -61 nm at 16%), evidencing an A × C interaction. This suggests that at higher viscosities (higher PET content), the system benefits more from additional electrostatic drawing to overcome jet resistance. PET content enlarged fibers (16%→20%: 379→502 nm, $\Delta \approx +122$ nm), which reflects the increase in solution viscosity and reduced extensional deformation of the jet. Flow-rate effects were concentration-dependent: at 16%, it rose from 0.6 to 1.2 mL·h^{-1} for thinned fibers (398→360 nm, $\Delta \approx -39$ nm), whereas at 20%, it thickened them (470→533 nm, $\Delta \approx +63$ nm), suggesting an A × B interaction (jet stability/evaporation). Consistent with the response surface (Figure 2a), PET shows a positive effect on diameter, while applied voltage shows a negative effect. The smallest experimental diameter (327 ± 173 nm) occurred at 16% content, 1.2 mL·h^{-1} flow rate, and 22 kV electric potential; center points (18%/0.9 mL·h^{-1}/19 kV) yielded large diameters (~600 ± 24 nm), indicating curvature and favoring higher field and lower concentration. Through Table 3, it was observed that the proposed model for the average diameter (σ), presented in Equation (7), is significant (p-value < 0.05), and the coefficient of determination (R^2) is 0.9878.

$$\sigma\ (\mu m) = 0.44 + 0.061A + 0.0058B - 0.077C + 0.026AB - 0.047AC \quad (7)$$

where A corresponds to the concentration of PET; B to the flow rate; C to the applied voltage; AB to the interaction between the concentration of PET and the flow rate; and AC to the interaction between the concentration of PET and the applied voltage.

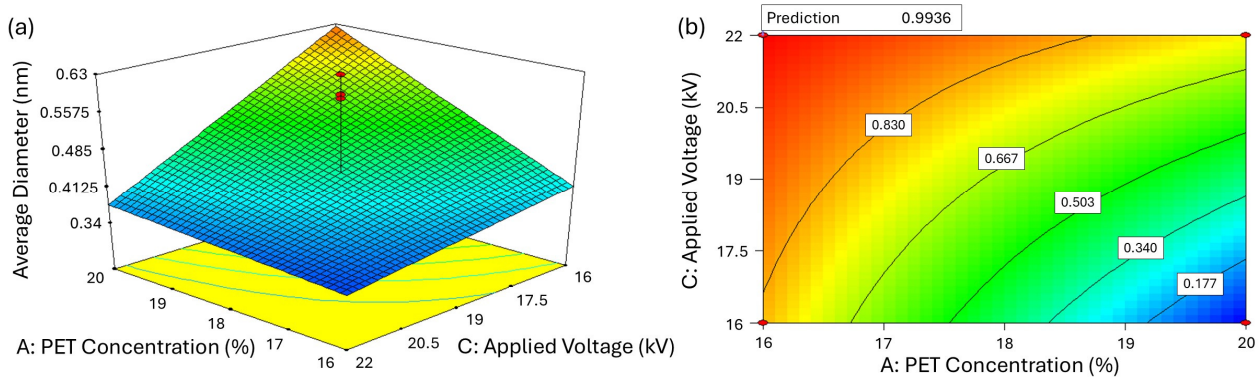


Figure 2. Response surface plot for the average diameter as a function of PET concentration and applied voltage (**a**) and a contour plot of desirability (**b**).

Table 3. ANOVA obtained for the response average diameter.

Source of Variations	Sum of Square	Degree of Freedom	Mean Square	F Statistics	*p*-Value
Model	0.10	5	0.020	64.60	0.0006
A—PET content	0.030	1	0.030	95.99	0.0006
B—Flow rate	2.668×10^{-4}	1	2.668×10^{-4}	0.85	0.4075
C—Applied voltage	0.048	1	0.048	153.14	0.0002
AB	5.233×10^{-3}	1	5.233×10^{-3}	16.76	0.0149
AC	0.018	1	0.018	56.25	0.0017
Curvature	0.056	1	0.056	177.97	0.0002
Residual	1.249×10^{-3}	4	3.121×10^{-4}	-	-
Lack of fit	9.593×10^{-5}	2	4.797×10^{-5}	0.083	0.9232
Pure error	1.153×10^{-3}	2	5.763×10^{-4}	-	-
Total	0.16	10	-	-	-

ANOVA confirmed global significance (F = 64.60, p = 0.0006), with applied voltage (C) the strongest main effect (F = 153.14, p = 0.0002), followed by PET content (A) (F = 95.99, p = 0.0006); flow rate (B) was not significant alone (F = 0.85, p = 0.4075). Interactions A × B (F = 16.76, p = 0.0149) and A × C (F = 56.25, p = 0.0017) were significant, curvature was pronounced (F = 177.97, p = 0.0002), and lack-of-fit was not (F = 0.083, p = 0.9232), supporting model adequacy. The variable with the greatest influence on average diameter was applied voltage (30.33%), followed by PET concentration (19.01%); flow rate contributed negligibly. Desirability-based optimization using Design-Expert® v7.0.0, targeting the minimum fiber diameter within the experimental range, identified 16% PET, 1.2 mL·h^{-1}, and 22 kV as the optimal conditions. The predicted diameter under these conditions was 0.33 µm, with an overall desirability of D = 0.994 (Figure 2b), consistent with the experimental minimum.

3.2. Viscosity of Polymeric Solutions

The viscosity of the polymer solution is a key parameter in the electrospinning process, as it dictates the level of polymer chain entanglement required to sustain a stable jet during elongation and solvent evaporation. Consequently, viscosity directly influences fiber diameter and morphology. Viscosities of PET solutions at different concentrations were measured, and the results are shown in Figure 3.

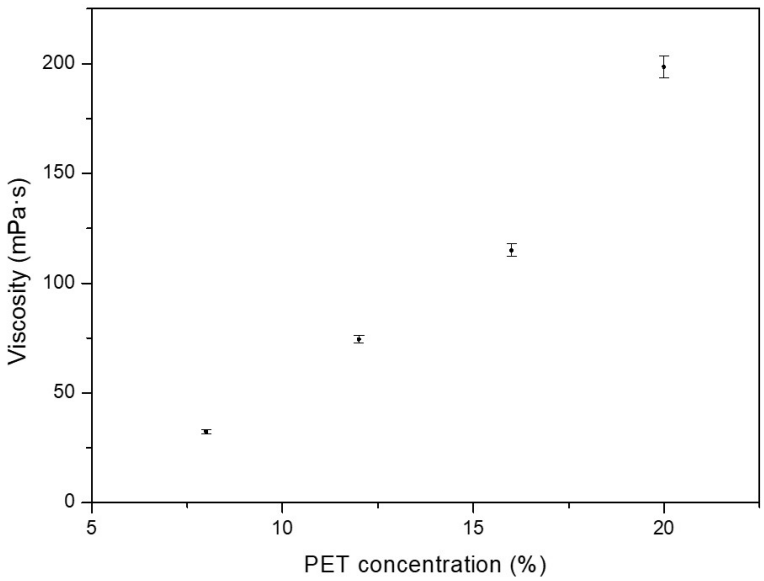


Figure 3. Viscosity as a function of PET concentration in solution. Mean viscosity values (dots) with ±standard deviation (error bars).

As expected, increasing PET concentration led to higher solution viscosities, which ranged from 32.35 to 198.5 mPa·s. Selatile et al. [48] reported viscosities of 280 and 180 mPa·s for 25% PET and 25% recycled PET, respectively. Mahalingam et al. [49] observed 25 mPa·s and 105 mPa·s for 10% and 20% PET solutions. Differences between the viscosities measured in this study and literature values can be attributed mainly to the type of PET used (virgin or recycled), the solvent and its composition, and the solution preparation method, including stirring time and environmental conditions.

Solutions with low viscosity, where chain entanglement is insufficient to sustain jet continuity, hinder electrospinning stability. Under these conditions, the jet is unable to remain cohesive during stretching, resulting in discontinuous fibers or a high density of beads, as observed in the SEM images of Figure 4a–c for 8%, 10%, and 12% PET solutions. Conversely, as viscosity increases with higher PET concentration, the stronger intermolecular entanglement stabilizes the jet, suppresses bead formation, and promotes

the formation of continuous fibers. However, when the viscosity becomes excessively high, jet stretching is restricted, which leads to thicker fibers and can even cause nozzle clogging or incomplete solvent evaporation, ultimately impairing fiber uniformity [50]. In general, higher solution viscosity correlates with larger fiber diameters, which is according to the studies of Bhardwaj and Kundu [51] and Keirouz et al. [52].

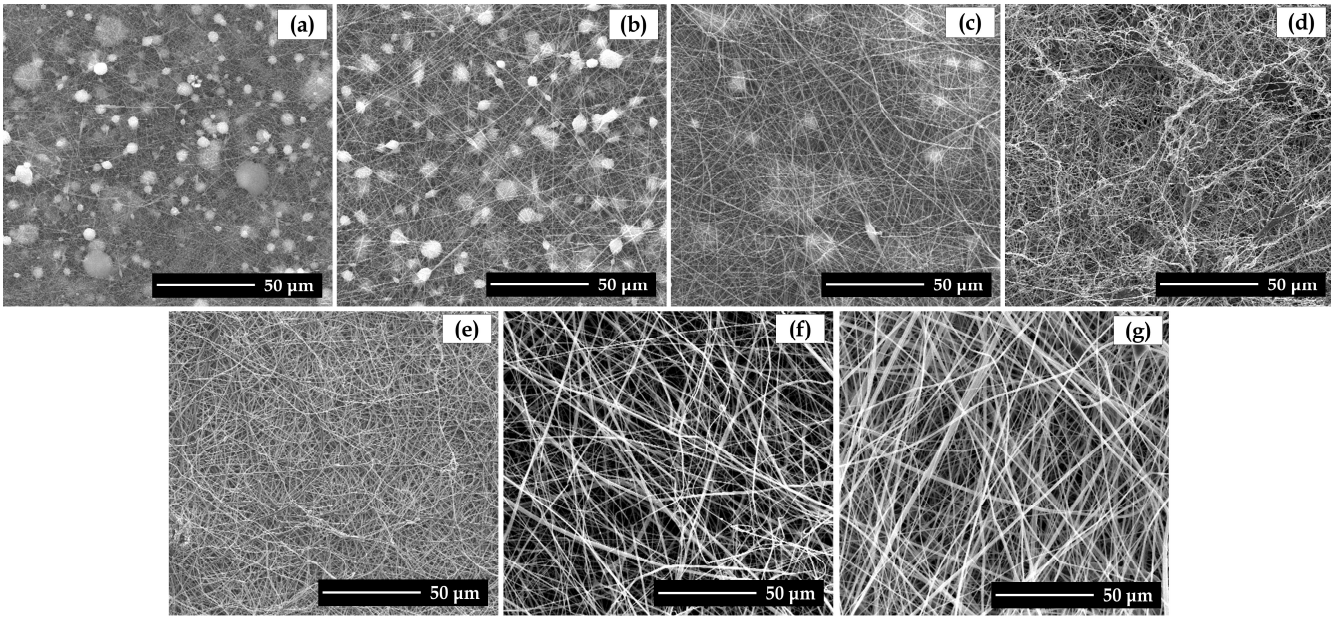


Figure 4. SEM images of the produced fibers from PET concentrations of 8% (**a**), 10% (**b**), 12% (**c**), 14% (**d**), 16% (**e**), 18% (**f**), and 20% (**g**).

3.3. Morphology and Diameter of PET Filter Media

Electrospinning parameters must be carefully controlled to produce nanofibers suitable for specific applications. Bead formation reduces fiber performance, weakening thermal and mechanical properties [53]; thus, process conditions should minimize bead formation.

Figure 4a–g presents SEM images of membranes produced from PET solutions at concentrations of 8, 10, 12, 14, 16, 18, and 20%, respectively. Whitish beads are visible in membranes with low PET concentrations. Increasing PET concentration from 8% to 12% reduces the number of beads along the fibers. Solutions with higher viscosities (Figure 3), obtained at PET concentrations above 16%, produced membranes with more uniform fibers and fewer beads. Fibers from solutions containing 8–12% PET displayed a high density of beads, whereas fibers containing 16–20% PET exhibited minimal bead formation.

This behavior is directly linked to polymer chain entanglement. At low concentrations, insufficient entanglement weakens the viscoelastic resistance of the jet, allowing capillary instabilities to dominate and resulting in bead-on-string morphologies [54]. As concentration increases, the higher viscosity strengthens jet cohesion and stabilizes elongational flow, preventing breakup and enabling continuous fiber formation [51,55]. This transition from bead-rich to uniform fibers is critical for filtration performance, as bead defects disrupt membrane homogeneity, create irregular pore networks, and can increase pressure drop while reducing capture efficiency. Therefore, the improved uniformity observed at 16–20% PET is directly associated with better-defined pore structure, enhanced mechanical integrity, and more favorable air-permeation behavior.

Using a rotating collector with a 10% PET solution prevented bead formation [29,31,32]. In contrast, when a flat plate collector was employed at the same concentration, beads were clearly observed (Figure 4b). These results are consistent with the findings of Abbas et al. [56] and Du et al. [30]. Thus, the type of collector plays a significant role in bead

formation at low polymer concentrations. The rotation of the collector promotes more uniform fiber deposition, providing a stable trajectory for fiber formation. Additionally, the stretching effect induced by a rotating collector aligns fibers more regularly, reducing irregularities that can lead to bead formation [57,58]. While a rotating collector promotes uniform fiber alignment, a flat collector has advantages for producing randomly oriented fibers, typically resulting in a more disordered deposition pattern [58,59]. This distinction is relevant for filtration, since randomly oriented mats produce a tortuous pore network that enhances interception and diffusion-based capture [9], whereas aligned mats are advantageous when directional mechanical reinforcement is desired [60].

Analysis of SEM images revealed that solutions with PET concentrations above 12% produced fibers without bead formation. Below this threshold, insufficient polymer chain entanglement results in bead-on-string morphologies, reflecting unstable jet behavior. Du et al. [30] reported similar results using a flat plate collector, showing that increasing PET concentration to 14% led to more uniform fiber diameters and fewer beads. In our system, concentrations of 16% and 20% PET yielded well-defined and bead-free fibers, consistent with the viscosity increase observed in Figure 3.

Based on these morphological observations, a 2^3 fractional factorial design was implemented to evaluate the effects of PET concentration, applied voltage, and solution flow rate on the average fiber diameter. The design focused on 16% and 20% PET solutions, as these concentrations fell within the regime where chain entanglement is sufficient to sustain stable fiber formation and minimize bead formation. Average fiber diameters obtained in experiments 1–11 are presented in Table 4, and representative SEM images with corresponding diameter distributions are shown in Figure 5.

Table 4. Values of the parameters used in the experiments generated by the fractional factorial design 2^3.

Experiments	PET Concentration (%)	Flow Rate (mL·h^{-1})	Applied Voltage (kV)	Average Diameter (nm)
1	16	0.6	16	427 ± 231
2	20	0.6	16	590 ± 254
3	16	1.2	16	392 ± 202
4	20	1.2	16	662 ± 244
5	16	0.6	22	370 ± 170
6	20	0.6	22	350 ± 135
7	16	1.2	22	327 ± 173
8	20	1.2	22	404 ± 165
9	18	0.9	19	590 ± 197
10	18	0.9	19	582 ± 196
11	18	0.9	19	627 ± 123

The smallest average diameter (327 nm) was observed in experiment 7, corresponding to 16% PET, 1.2 mL·h^{-1}, and 22 kV. In contrast, the largest average diameter (661 nm) was obtained in experiment 4, using 20% PET, 16 kV, and a flow rate of 1.2 mL·h^{-1}. These trends are consistent with the known relationship between viscosity and electrostatic drawing: higher polymer concentrations increase viscosity, which tends to produce thicker fibers unless higher electric forces are applied [61,62].

Environmental conditions (38–46% relative humidity and 20–25 °C) were monitored but did not vary significantly enough to influence fiber morphology within the experimental range and therefore were not included as independent variables.

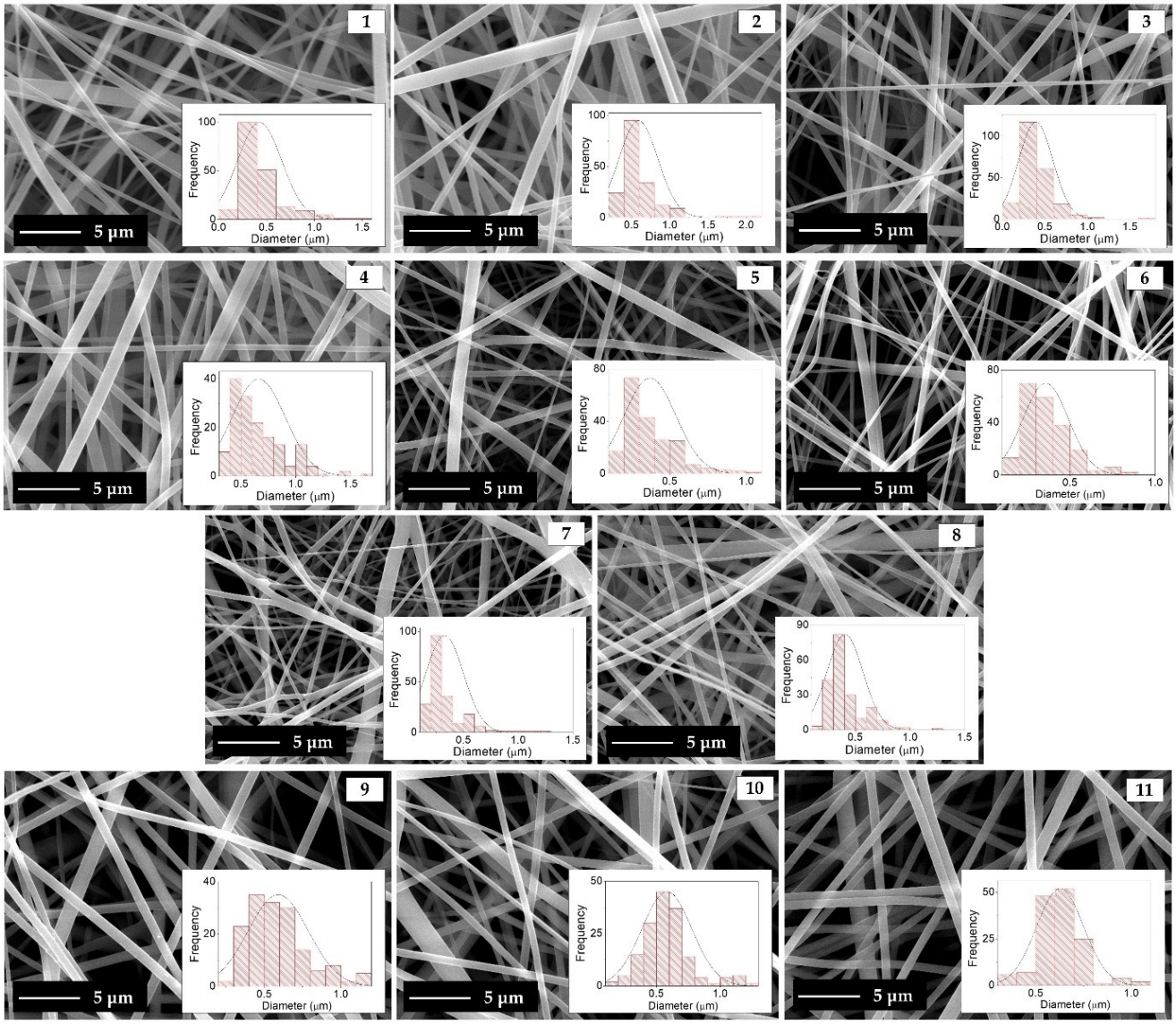


Figure 5. SEM images and histograms of diameter distribution of PET fibers collected during electrospinning under the conditions of experiments 1 to 11 (Table 4). Bars represent the experimental distribution and the line indicates the fitted normal distribution.

3.4. Characterization of PET Filter Media

Figure 6 shows the FTIR spectra of the membranes obtained from PET at concentrations of 8, 12, 14, 16, and 20%, as well as the PET bottle used to produce polymeric solutions. The spectra exhibit the main characteristic bands of PET (2958 cm^{-1}, 1716 cm^{-1}, 1242 cm^{-1}, 1095 cm^{-1}, and 725 cm^{-1}), as evidenced in the spectrum of the PET bottle [29].

The band at 2958 cm^{-1} corresponds to axial C–H vibrations in the aromatic structure of the polymer. The bands at 1716 cm^{-1}, 1242 cm^{-1}, and 1095 cm^{-1} are assigned to the ester carbonyl stretching (C=O) of terephthalate, ester (C=O)–C stretching, and ester C–O stretching (C=O/O–CH_2), respectively—typical PET features. At 725 cm^{-1}, oscillating C–H vibrations of aromatic rings are observed; similarly, the bands at 1016 cm^{-1} and 1043 cm^{-1} arise from in-plane C–H deformations (gauche conformation), with 1016 cm^{-1} also reflecting interactions within the aromatic ring. A band at 1407 cm^{-1} corresponds to in-plane C–H ring deformation, and at 872 cm^{-1} a planar C–H vibration of the aromatic ring is evident. Overall, the bands at 1716 and 1095 cm^{-1} are characteristic of PET, while

725/1016 cm^{-1} can be associated with interactions within the aromatic rings alongside C–H deformations [29,48,63].

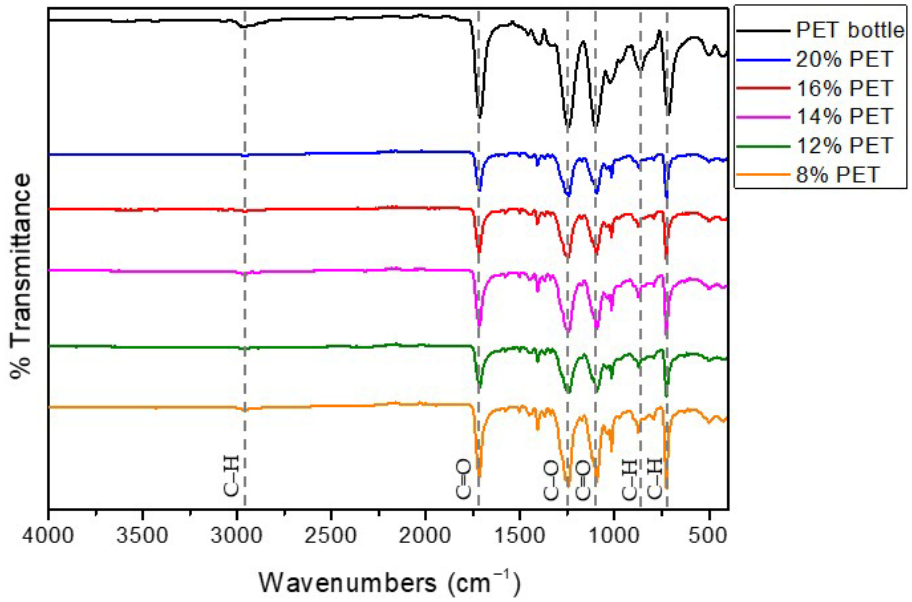


Figure 6. The FTIR spectra of the membranes obtained via electrospinning from PET solutions with concentrations of 8%, 12%, 14%, 16%, and 20%, as well as the PET bottle.

Kijeńska-Gawrońska et al. [64] compared electrospun mats made from recycled PET (rPET) and virgin PET (vPET), showing that both exhibited similar characteristic absorption bands. This indicates that the fundamental chemical structure of PET is preserved during recycling and electrospinning. Differences in band intensities are mainly due to variations in ATR measurement depth and region. The spectra also confirm the absence of residual solvents in the fibers. According to Strain et al. [29], for TFA, the C–F stretching bands appear between 1250 and 1180 cm^{-1}, while the symmetric and asymmetric stretching of the C–Cl bond of DCM is located at 874 and 771 cm^{-1}. These results demonstrate that rPET maintains chemical integrity and stability, supporting its use for high-quality electrospun materials with properties comparable to virgin PET.

Figure 7a presents the DSC curves for membranes with 8, 12, 14, 16, and 20% PET, as well as the PET bottle used to prepare the solutions. From the DSC curves, the glass transition temperature (Tg), melting temperature (Tm), and cold crystallization temperature (Tcc) were determined for each sample. The PET bottle exhibited a Tg of 78.5 °C, consistent with literature values [27]. In the electrospun fibers, Tg was obscured by an endothermic peak, but no significant deviation from the PET bottle value was observed, with only a slight increase due to the higher amorphous content in the fibers (Table 5).

Table 5. Data obtained from the DSC curves and the degree of crystallinity for the PET bottle and the membranes of 8%, 12%, 14%, 16%, and 20% PET.

Sample	Tg (°C)	Tm (°C)	ΔHm (J·g^{-1})	Tcc (°C)	ΔHcc (J·g^{-1})	χ_c (%)
8% PET	83.31	248.06	44.53	137.06	17.39	19.99
12% PET	81.84	246.02	37.59	133.23	15.80	16.05
14% PET	83.17	246.50	40.06	133.65	19.24	15.33
16% PET	81.30	245.82	38.35	129.29	19.47	13.90
20% PET	81.05	244.06	32.47	127.78	19.01	9.912
PET bottle	78.51	247.08	49.72	-	0	36.61

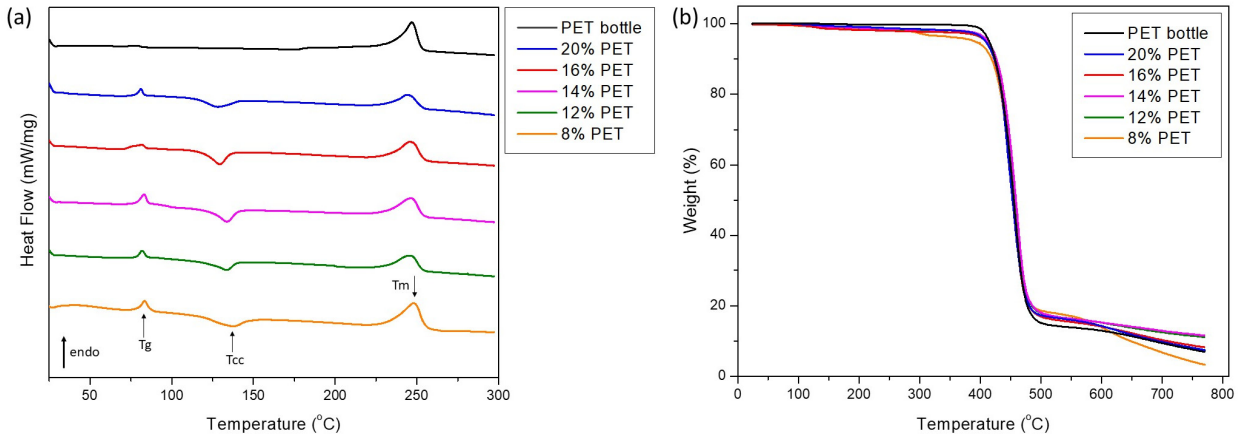


Figure 7. DSC curves of the PET bottle (black curve) and electrospun membranes with PET concentrations of 8% (orange), 12% (green), 14% (pink), 16% (red), and 20% (blue). The main thermal transitions are indicated: Tg—glass transition (~78.5 °C for the PET bottle), Tcc—cold crystallization, and Tm—melting (**a**); TG curves of the PET bottle (black curve) and membranes obtained via electrospinning from PET solutions with concentrations of 8% (orange curve), 12% (green curve), 14% (pink curve), 16% (red curve), and 20% (blue curve) (**b**).

The endothermic and exothermic peaks corresponded to Tm and ΔHm, and Tcc and ΔHcc, respectively. These values for each sample are listed in Table 5. The degree of crystallinity (χ_c) of the samples was calculated using Equation (8):

$$\chi_C(\%) = \frac{\Delta H_m - \Delta H_{cc}}{\Delta H_m^0} \times 100\% \quad (8)$$

where ΔH_m is the melting enthalpy, ΔH_{cc} is the crystallization enthalpy, and $\Delta {H_m}^0$ is the melting enthalpy for 100% crystalline PET. According to Veleirinho et al. [27], $\Delta {H_m}^0$ for PET is 135.8 J·g^{-1}. The χ_c values are summarized in Table 5.

Celik et al. [65] studied the thermal and mechanical properties of recycled PET (rPET) compared with virgin PET (vPET). They reported Tg values for rPET ranging from 78.3 to 81.2 °C, slightly lower than those of vPET (69–115 °C), primarily due to the lower molecular weight of rPET, which affects chain-end concentration and polymer free volume. This highlights the importance of careful recycling to ensure rPET maintains quality comparable to vPET for applications requiring high thermal resistance. Despite slight differences, rPET meets quality standards when processed appropriately.

The values of Tm and Tcc fall within the range reported in the literature [48,66]. A slight decrease in Tm was observed with increasing PET concentration, which can be attributed to the formation of less perfect crystals [67]. This behavior is consistent with previous reports on electrospun polymer fibers, where rapid solidification, larger fiber diameters, and reduced chain alignment during jet stretching led to lower crystallinity and, consequently, reduced melting temperature [67,68]. The variations observed in ΔHm and ΔHcc across different PET concentrations are attributed to heterogeneities in fiber morphology and internal structure induced by the electrospinning process. Rapid solvent evaporation and uneven jet stretching lead to fibers with non-uniform diameters and degrees of crystallinity, resulting in fluctuations in melting and crystallization enthalpies, even for samples with similar PET content.

The degree of crystallinity (χ_c) decreased with increasing PET concentration in the solution, from 19.99% for 8% PET to 9.91% for 20% PET. This trend indicates that higher polymer concentrations lead to less chain alignment and organization during electrospinning, resulting in fibers with lower crystallinity. The χ_c for the PET bottle was 36.61%,

higher than the value of 21.2% found by Strain et al. [29] and higher than the values found for the fibers. In a study, Viora et al. [69] conducted a comparative analysis of the crystallization behavior of vPET and rPET, focusing on how the Tcc influences their physico-mechanical properties. The research involved analyzing three types of materials: vPET, rPET, and a 50/50 blend of recycled and virgin PET (50rPET). The study demonstrates that rPET exhibits a higher Tcc compared to vPET, which is attributed to the presence of shorter polymer chains and contaminants that act as nucleating agents, promoting more efficient crystallization. The alterations in Tcc can be attributed to these factors, as they influence the polymer's ability to crystallize during thermal processing.

Thermogravimetric analysis (Figure 7b) revealed a single major mass loss stage for all samples, occurring between 350 and 550 °C, with Tonset around 430 °C. The corrected mass loss percentages ranged from 88.43% to 96.79%, indicating that all membranes, regardless of PET content, maintained thermal stability comparable to the PET bottle.

3.5. Performance of PET Filter Media

The performance of the filter media was evaluated based on two parameters: air permeability and filtration efficiency for nanoscale particles. These parameters are essential for assessing the effectiveness of filters in air purification, especially in retaining small-sized particles. Membranes containing 8% and 12% PET were produced under conditions of 0.6 mL·h^{-1} flow rate, 16 kV applied voltage, and 8 cm tip-to-collector distance. Meanwhile, the membranes with 16 and 20% PET were produced under the conditions of 1.2 mL·h^{-1}, 22 kV, and 12 cm, corresponding to the factorial design conditions that yielded the smallest average fiber diameters, as smaller fibers are generally more efficient for filtration [32].

Random fiber orientation can be advantageous in air filtration [37,40]. Berry et al. [37] reported that media with randomly arranged fibers exhibit higher permeability than ordered fiber mats. Cai et al. [40] showed that fiber orientation significantly affects particle collection via interception and inertial impaction but has less impact on diffusion-dominated capture. Nanoparticle capture is primarily governed by Brownian diffusion, which is more effective in a network of randomly oriented fibers, as particles have more opportunities to collide with fibers. Consequently, randomly oriented fibers create a tortuous path for airflow, enhancing filtration efficiency, particularly for fine and ultrafine particles. This highlights the benefits of using a flat plate collector in filter production.

Permeability constants (k_1) were determined using Darcy's equation (Equation (4)), as filtration velocities were low. Airflow rates ranged from 0.3 to 6.4 cm·s^{-1}, and the pressure drop (ΔP) was measured at each flow rate (Figure 8) for PET concentrations of 8%, 12%, 16%, and 20%. The permeability constant (k_1) for the filter media is shown in Table 6. The permeability increased with PET concentration—and thus with fiber diameter. Consistent with this trend, Park and Park [70] reported that the air permeability of electrospun nylon 6,6 membranes decreases as fiber size is reduced. The magnitude of k_1 agrees with literature values [33,71]; for example, Bortolassi et al. [42] reported $k_1 = (7.28–9.62) \times 10^{-13}$ for HEPA filters, higher than that of the 20% PET media.

Comparing the permeability of the filter media from 8 to 16%, it is noted that the filter media produced with higher PET concentrations showed practically the same collection efficiency as the filter media with lower concentrations, but with higher permeability and lower pressure drop. Thus, the filter media with 16% PET can be considered the one with the lowest energy consumption compared to the others. The 16% PET filter exhibited a higher pressure drop than the 20% PET, indicating that increasing polymer concentration yields media with lower ΔP—and thus lower airflow resistance, a similar result to that found by Abuzade et al. [72].

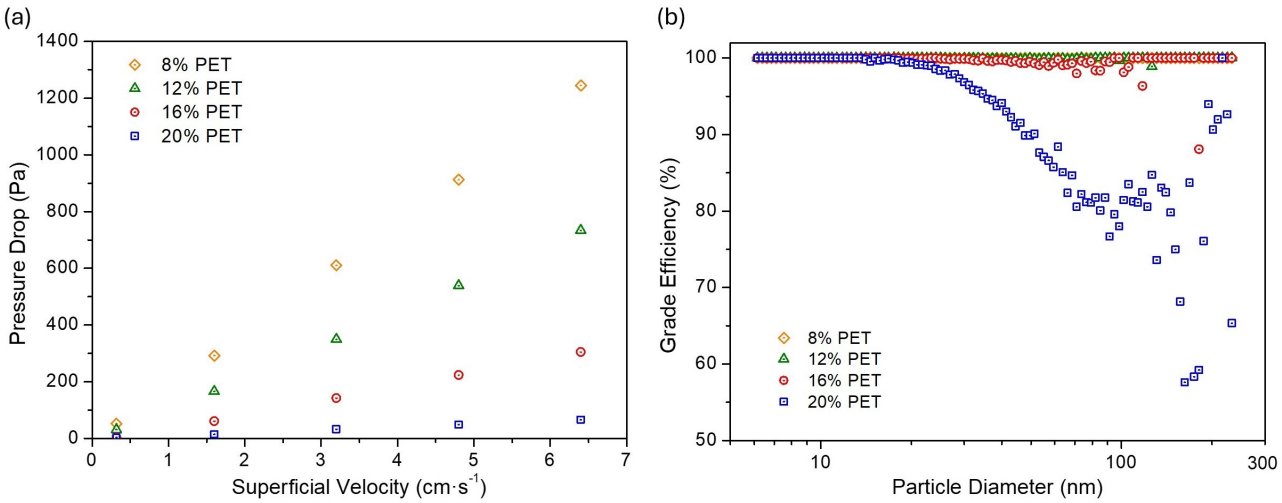


Figure 8. (**a**) Relationship between pressure drop and superficial velocity for nanofiber filter media fabricated with varying PET concentrations. (**b**) Grade efficiency of the filters as a function of particle diameter.

Table 6. Pressure drops (ΔP) (at face velocity of 4.8 cm·s^{-1}), permeability constant (k_1), efficiency, and quality factors (Q_f) of the developed filter media at different PET concentrations.

PET Concentration (%)	Pressure Drop (Pa)	k_1 (m^2)	Efficiency (%)	Quality Factor (Pa^{-1})
8	912.4 ± 0.9	1.15×10^{-13}	99.99 ± 0.00	0.0043
12	538.7 ± 1.9	1.63×10^{-13}	99.95 ± 0.01	0.0063
16	223.4 ± 0.8	3.19×10^{-13}	99.77 ± 0.04	0.0272
20	48.5 ± 0.4	1.07×10^{-12}	95.65 ± 0.03	0.0646

Studies in the literature, as reported by Xia et al. [12], indicate a range of pressure drops from 80.5 to 346.0 Pa for 20% PET. These results were obtained considering a superficial velocity range of 5 to 20 cm·s^{-1}. Bonfim et al. [32] obtained pressure drop values of 76.1, 212.5, and 13.5 Pa for filter media with 10%, 12%, and 20% recycled PET, respectively, at an air flow rate of 4.8 cm·s^{-1}, using the following parameters: rotating collector, flow rate of 0.8 mL·h^{-1}, distance of 10 cm, and 20 kV of electrical field potential. Ng et al. [73] produced 10% recycled PET filter media with a pressure drop of 39.2 Pa at 13 cm·s^{-1}, using a rotating collector, 0.6 mL·h^{-1} flow rate, 19 cm tip-to-collector distance, and 20 kV.

At a comparable face velocity of 4.8 cm·s^{-1}, the 20% PET membrane outperformed these references, with ΔP = 48.5 Pa, demonstrating effective parameter optimization. Higher pressure drops in lower-concentration membranes can be attributed to the larger number of beads, which obstruct airflow. Specifically, at 4.8 cm·s^{-1}, the 8% and 12% PET media had ΔP below the HEPA range (269–418 Pa) [42]; the 16% PET filter media was near the lower end of HEPA values (223.4 Pa), while the 20% PET filter media exhibited a significantly lower ΔP (48.5 Pa).

The overall filtration efficiency for nanoparticle capture was nearly 100% for the 16% PET filter. In contrast, the 20% PET filter, having larger fiber diameters, exhibited slightly lower efficiency due to the reduced effectiveness of diffusion-driven capture mechanisms, highlighting the critical role of fiber diameter in nanoscale particle retention. As reported by Park and Park [70], smaller fiber diameters increase the membrane's specific surface area, enhancing particle capture. Additionally, slip flows around fine fibers improve interception and inertial impaction, further boosting filtration performance [41]. In this work, filters with low bead content (16% and 20% PET) performed similarly in efficiency, while 8% and 12% PET filters still exceeded HEPA standards, with efficiencies above 99.95% [71].

Literature reports support the use of PET nanofibers for air filtration. Using flat plate collectors, Šišková et al. [28] obtained filters from 10% recycled PET, achieving 99.95% and 98.28% efficiency for 0.6 µm and 120 nm particles, respectively. Du et al. [30] electrospun 14% PET onto a PET screen, reaching 87% efficiency for particles < 2.5 µm with 20 min of spinning. With rotary collectors, Bonfim et al. [32] obtained 99% efficiency for 7–300 nm particles using 10–12% PET, while Hossain et al. [35] reported 97.04% efficiency for 0.3 µm particles with 20% PET membranes.

Considering quality factors relative to HEPA filters (0.010 and 0.011 Pa^{-1}) [74], the 16% and 20% PET membranes showed higher values, 0.027 Pa^{-1} and 0.065 Pa^{-1}, respectively. Thus, the 20% PET filter showed the highest quality factor. Although the other filters have better filtration efficiency than a 20% PET sample, their quality factors are lower. This fact can be explained by the higher pressure drop presented in the filtration tests of the 8%, 12%, and 16% PET filters, highlighting the importance of evaluating both efficiency and airflow resistance in filter performance. Bonfim et al. [32] obtained the same quality factor value (0.06 Pa^{-1}) for a fiber with 10% PET. Although the quality factor is the same, the diameters and arrangements of the fibers differ because the conditions used, such as the type of collector, are not the same. Considering the same polymer concentration, 10% PET, Ng et al. [73] produced filter media with a quality factor of 0.019 Pa^{-1}. Bortolassi et al. [71] also obtained filter media with similar quality factors (0.04 Pa^{-1} and 0.06 Pa^{-1}) for a flow rate of 1500 $cm^3 \cdot min$ for PAN nanofibers. Xia et al. [12] presented a summary of studies in the literature regarding quality factors obtained for different polymeric nanofibers. The highest values were found for polysulfone (PSU) membranes, with 0.26 Pa^{-1}, while the lowest values were observed for polyimide (PI), with 0.01 Pa^{-1}. These values are related to air velocity and filtration efficiency, considering a specific range of particle diameters.

Recent studies reinforce the versatility of rPET in air filtration. Lima et al. [75] produced hybrid media from recycled PET and polystyrene (rPET + rPS) and, in line with our findings, showed that increasing the rPET fraction enhanced nanoparticle (6.38–232.9 nm) capture while keeping ΔP far below HEPA values. Shu et al. [76] electrospun luminescent PET nano-woven filters under dual high-voltage fields, incorporating a rare-earth complex so the membrane functioned as both filter and sensor; their dual-scale network achieved 82% porosity, 106 Pa pressure drop, and 99% removal from PM5.0 down to PM0.3. Deng et al. [77] proposed a 3D "fluffy" gradient architecture by depositing nano-PLA fibers onto recycled, curved R-PET microfiber webs (linear, S-shaped, and zigzag) and, without using electret PP, optimized PET curvature and PLA basis weight to balance efficiency and airflow; with NaCl aerosol (260 nm, 5.3 $cm \cdot s^{-1}$), the zigzag R-PET + nano-PLA mat reached 99.99% efficiency at 200 Pa and the highest quality factor (0.047 Pa^{-1}), because the curved 3D scaffold created slip-flow paths while the nanofiber layer trapped the fine particles. These examples emphasize that fiber morphology, arrangement, and multi-scale architecture can be strategically engineered to optimize both filtration efficiency and air permeability.

3.6. Porosity Analysis

Porosity was theoretically determined using the Davies relation (Equation (4)) and experimentally via two independent methods (Equations (5) and (6)). Table 7 reports the results from all three formulations—expressed as percentages (i.e., $\varphi \times 100\%$)—for electrospun fibers prepared with different PET concentrations.

Theoretical porosity ranged from 96.47% to 98.73%, whereas experimental porosity ranged from 75.98% to 92.52% across the two methods. The mean deviation of experimental porosity (Equation (5)) from the theoretical value was 5%, 6%, 3%, and 3% for the 8%, 12%, 16%, and 20% PET membranes, respectively. Using Equation (6), the corresponding mean deviations were 11%, 8%, 2%, and 2% for 8%, 12%, 16%, and 20% PET, respectively.

Table 7. Theoretical and experimental porosity (%) of electrospun PET fibers determined by the Davies relation and two experimental methods.

PET Concentration (%)	Theoretical Porosity (%) [1]	Experimental Porosity (%) [2]	Experimental Porosity (%) [3]
8	98.73 ± 0.01	88.64 ± 0.01	75.98 ± 0.05
12	98.18 ± 0.01	86.12 ± 0.01	81.53 ± 0.01
16	95.96 ± 0.04	89.86 ± 0.01	91.52 ± 0.00
20	96.47 ± 0.02	90.35 ± 0.01	92.52 ± 0.01

[1] Obtained by Equation (4) (Davies). [2] Obtained by Equation (5) (sample weight). [3] Obtained by Equation (6) (butyric alcohol absorption).

Among the PET membranes, the 20% PET filter media showed the highest experimental porosity across both measurement methods. The theoretically calculated porosity range is consistent with literature reports for electrospun nanofibers using the same equation [45].

Analyzing the data in Table 7, increasing PET concentration decreases theoretical porosity, as expected: thinner fibers tend to yield a larger void fraction and more homogeneous pore structures, thus increasing porosity. However, this trend contrasts with the experimental results, in which lowering the PET concentration is associated with a decrease in porosity. This discrepancy highlights the limitations of relying solely on theoretical models, which do not fully capture the complex microstructure of electrospun mats, particularly when bead formation and fiber diameter heterogeneity are present.

As noted earlier, increasing PET concentration correlates with higher permeability and lower pressure drop in the filter media. Accordingly, porosity would be expected to be greater in filters with higher permeability—i.e., at higher polymer concentrations. This expectation is confirmed by the experimental values obtained by both methodologies, indicating that the Davies relation did not adequately represent the 8% and 12% PET membranes. A plausible explanation is that the Davies equation places disproportionate weight on fiber radius while underweighting pressure-drop effects, leading to misinterpretation—especially when it ignores bead diameters present in fibers produced at lower polymer concentrations.

Overall, these results emphasize that experimental assessment of porosity is essential for accurately characterizing electrospun filter media. The findings also suggest that optimizing polymer concentration not only influences fiber morphology but also directly affects the effective void space, which is critical for filtration performance and fluid transport properties. This reinforces the practical importance of considering both morphological heterogeneity and theoretical limitations when designing high-efficiency nanofibrous membranes.

4. Conclusions

This study concluded that filter media can be produced more efficiently by optimizing operational settings from electrospinning a recyclable PET solution. The concentration of PET and the applied voltage were identified as the key variables influencing the average diameter of the fibers produced. Nanofibers with minimal bead formation were observed at higher PET concentrations (16% and 20%). The smallest average diameter of 330 nm was achieved with a 16% PET concentration, a flow rate of 1.2 mL·h^{-1}, and an applied voltage of 22 kV.

Porosity measurements revealed that increasing PET concentration enhanced the experimental void fraction, correlating with higher air permeability and lower pressure drop. Although higher PET concentration resulted in larger average fiber diameters, it also improved permeability while slightly reducing nanoparticle collection efficiency. Notably, nanofibers with 20% PET exhibited a low-pressure drop of 48.5 Pa, while those with 16% PET had a pressure drop of 223 Pa, both of which are lower than the values reported for

HEPA filters under similar conditions. In this way, even using more PET concentration to produce nanofibers with better air filtration performance is not a burden since the source of the polymer is solid waste generated abundantly.

We expect the findings in this article to assist in the design of more efficient and sustainable air filtration devices. They provide insights into developing filters that have been optimized for indoor environments to effectively capture nanoparticles, thereby enhancing the health and well-being of people who are exposed to air pollution.

Author Contributions: Conceptualization, G.B.M., D.S.d.A. and M.L.A.; methodology, G.B.M., P.A.M.C., D.P.F.B. and G.C.d.M.; formal analysis, G.B.M. and D.S.d.A.; investigation, G.B.M., P.A.M.C., D.P.F.B. and G.C.d.M.; resources, M.L.A.; data curation, G.B.M. and M.L.A.; writing—original draft preparation, G.B.M.; writing—review and editing, G.B.M., P.A.M.C., D.P.F.B., G.C.d.M., D.S.d.A. and M.L.A.; visualization, G.B.M.; supervision, D.S.d.A. and M.L.A.; project administration, M.L.A.; funding acquisition, M.L.A. All authors have read and agreed to the published version of the manuscript.

Funding: This research was funded by the Coordination for the Improvement of Higher Education Personnel (CAPES Financing Code 001 within the Graduate Program in Chemical Engineering at Federal University of São Carlos, Grant 88887.505019/2020-00 and Scholarship 88887.124941/2025-00), the National Council for Scientific and Technological Development (CNPq—Grant 424792/2018-4 and Scholarship 140704/2023-0), and the São Paulo Research Foundation (FAPESP—Grant 2023/18068-2; 2023/05407-3; 2024/19619-5 and 2026/00734-4). The authors acknowledge the financial support of CAPES, CNPq, and FAPESP.

Data Availability Statement: The original contributions presented in this study are included in the article. Further inquiries can be directed to the corresponding authors.

Acknowledgments: The authors would like to thank the Environmental Control Laboratory (LCA) of the Department of Chemical Engineering (DEQ/UFSCar), the Structural Characterization Laboratory (LCE) of the Department of Materials Engineering (DEMa/UFSCar), and the Pharmaceutical Technology Laboratory (FCFRP/USP).

Conflicts of Interest: The authors declare no conflicts of interest.

References

1. Petrowski, K.; Bührer, S.; Strauß, B.; Decker, O.; Brähler, E. Examining Air Pollution (PM_{10}), Mental Health and Well-Being in a Representative German Sample. *Sci. Rep.* **2021**, *11*, 18436. [CrossRef]
2. Shang, Y.; Liu, M.; Wang, T.; Wang, L.; He, H.; Zhong, Y.; Qian, G.; An, J.; Zhu, T.; Qiu, X.; et al. Modifications of Autophagy Influenced the Alzheimer-like Changes in SH-SY5Y Cells Promoted by Ultrafine Black Carbon. *Environ. Pollut.* **2019**, *246*, 763–771. [CrossRef] [PubMed]
3. Zhang, J.; Chen, Z.; Shan, D.; Wu, Y.; Zhao, Y.; Li, C.; Shu, Y.; Linghu, X.; Wang, B. Adverse Effects of Exposure to Fine Particles and Ultrafine Particles in the Environment on Different Organs of Organisms. *J. Environ. Sci.* **2024**, *135*, 449–473. [CrossRef] [PubMed]
4. Chen, R.; Hu, B.; Liu, Y.; Xu, J.; Yang, G.; Xu, D.; Chen, C. Beyond $PM_{2.5}$: The Role of Ultrafine Particles on Adverse Health Effects of Air Pollution. *Biochim. Biophys. Acta—Gen. Subj.* **2016**, *1860*, 2844–2855. [CrossRef] [PubMed]
5. OMS Air Pollution. Available online: https://www.who.int/health-topics/air-pollution#tab=tab_1 (accessed on 13 June 2025).
6. Robert, B.; Nallathambi, G. A Concise Review on Electrospun Nanofibres/Nanonets for Filtration of Gaseous and Solid Constituents ($PM_{2.5}$) from Polluted Air. *Colloids Interface Sci. Commun.* **2020**, *37*, 100275. [CrossRef]
7. Baby, T.; Jose, T.E.; Aravindkumar, C.T.; Thomas, J.R. A Facile Approach for the Preparation of Polycarbonate Nanofiber Mat with Filtration Capability. *Polym. Bull.* **2020**, *78*, 3363–3381. [CrossRef]
8. Zhang, S.; Rind, N.A.; Tang, N.; Liu, H.; Yin, X.; Yu, J.; Ding, B. Electrospun Nanofibers for Air Filtration. In *Electrospinning: Nanofabrication and Applications*; Elsevier Inc.: Amsterdam, The Netherlands, 2019; pp. 365–389.
9. Russo, F.; Castro-Muñoz, R.; Santoro, S.; Galiano, F.; Figoli, A. A Review on Electrospun Membranes for Potential Air Filtration Application. *J. Environ. Chem. Eng.* **2022**, *10*, 108452. [CrossRef]
10. Lu, T.; Cui, J.; Qu, Q.; Wang, Y.; Zhang, J.; Xiong, R.; Ma, W.; Huang, C. Multistructured Electrospun Nanofibers for Air Filtration: A Review. *ACS Appl. Mater. Interfaces* **2021**, *13*, 23293–23313. [CrossRef]

11. Sambaer, W.; Zatloukal, M.; Kimmer, D. 3D Air Filtration Modeling for Nanofiber Based Filters in the Ultrafine Particle Size Range. *Chem. Eng. Sci.* **2012**, *82*, 299–311. [CrossRef]
12. Xia, T.; Bian, Y.; Zhang, L.; Chen, C. Relationship between Pressure Drop and Face Velocity for Electrospun Nanofiber Filters. *Energy Build.* **2018**, *158*, 987–999. [CrossRef]
13. Konda, A.; Prakash, A.; Moss, G.A.; Schmoldt, M.; Grant, G.D.; Guha, S. Aerosol Filtration Efficiency of Common Fabrics Used in Respiratory Cloth Masks. *ACS Nano* **2020**, *14*, 6339–6347. [CrossRef] [PubMed]
14. Wang, X.X.; Yu, G.F.; Zhang, J.; Yu, M.; Ramakrishna, S.; Long, Y.Z. Conductive Polymer Ultrafine Fibers via Electrospinning: Preparation, Physical Properties and Applications. *Prog. Mater. Sci.* **2021**, *115*, 100704. [CrossRef]
15. Rezić Meštrović, I.; Somogyi Škoc, M. Nanofiber-Based Innovations in Energy Storage Systems. *Polymers* **2025**, *17*, 1456. [CrossRef] [PubMed]
16. Xu, C.; Tan, J.; Li, Y. Application of Electrospun Nanofiber-Based Electrochemical Sensors in Food Safety. *Molecules* **2024**, *29*, 4412. [CrossRef]
17. Akhavan-Mahdavi, S.; Mirbagheri, M.S.; Assadpour, E.; Sani, M.A.; Zhang, F.; Jafari, S.M. Electrospun Nanofiber-Based Sensors for the Detection of Chemical and Biological Contaminants/Hazards in the Food Industries. *Adv. Colloid Interface Sci.* **2024**, *325*, 103111. [CrossRef]
18. Guerrero-Pérez, M.O. Research Progress on the Applications of Electrospun Nanofibers in Catalysis. *Catalysts* **2021**, *12*, 9. [CrossRef]
19. Partovi, A.; Khedrinia, M.; Arjmand, S.; Ranaei Siadat, S.O. Electrospun Nanofibrous Wound Dressings with Enhanced Efficiency through Carbon Quantum Dots and Citrate Incorporation. *Sci. Rep.* **2024**, *14*, 19256. [CrossRef]
20. Zhang, X.; Wang, Y.; Gao, Z.; Mao, X.; Cheng, J.; Huang, L.; Tang, J. Advances in Wound Dressing Based on Electrospinning Nanofibers. *J. Appl. Polym. Sci.* **2024**, *141*, e54746. [CrossRef]
21. Shang, Z.; Wycisk, R.; Pintauro, P. Electrospun Composite Proton-Exchange and Anion-Exchange Membranes for Fuel Cells. *Energies* **2021**, *14*, 6709. [CrossRef]
22. Mata, G.C.D.; Morais, M.S.; Oliveira, W.P.D.; Aguiar, M.L. Composition Effects on the Morphology of PVA/Chitosan Electrospun Nanofibers. *Polymers* **2022**, *14*, 4856. [CrossRef]
23. Ji, D.; Lin, Y.; Guo, X.; Ramasubramanian, B.; Wang, R.; Radacsi, N.; Jose, R.; Qin, X.; Ramakrishna, S. Electrospinning of Nanofibres. *Nat. Rev. Methods Prim.* **2024**, *4*, 1. [CrossRef]
24. Aragaw, T.A. Surgical Face Masks as a Potential Source for Microplastic Pollution in the COVID-19 Scenario. *Mar. Pollut. Bull.* **2020**, *159*, 111517. [CrossRef] [PubMed]
25. Lima, F.D.A.; Chagas, P.A.M.; Honorato, A.C.S.; da Silva, E.N.; Aguiar, M.L.; Guerra, V.G. Multifactorial Evaluation of an Ultra-Fast Process for Electrospinning of Recycled Expanded Polystyrene to Manufacture High-Efficiency Membranes for Nanoparticle Air Filtration. *J. Environ. Manag.* **2024**, *362*, 121352. [CrossRef] [PubMed]
26. da Silva, E.N.; Chagas, P.A.M.; de Aquino Lima, F.; de Souza, C.W.O.; Aguiar, M.L.; Guerra, V.G. Development of Bifunctional Electrospun Filters Incorporating Surfactants for Enhanced Particulate Matter Filtration and Antimicrobial Activity. *Fibers Polym.* **2024**, *25*, 4227–4243. [CrossRef]
27. Veleirinho, B.; Rei, M.F.; Lopes-da-Silva, J.A. Solvent and Concentration Effects on the Properties of Electrospun Poly(Ethylene Terephthalate) Nanofiber Mats. *J. Polym. Sci. Part B Polym. Phys.* **2008**, *46*, 460–471. [CrossRef]
28. Šišková, A.O.; Frajová, J.; Nosko, M. Recycling of Poly(Ethylene Terephthalate) by Electrospinning to Enhanced the Filtration Efficiency. *Mater. Lett.* **2020**, *278*, 128426. [CrossRef]
29. Strain, I.N.; Wu, Q.; Pourrahimi, A.M.; Hedenqvist, M.S.; Olsson, R.T.; Andersson, R.L. Electrospinning of Recycled PET to Generate Tough Mesomorphic Fibre Membranes for Smoke Filtration. *J. Mater. Chem. A* **2015**, *3*, 1632–1640. [CrossRef]
30. Du, L.; Zhang, Y.; Li, X.; Wang, J.; Chen, M.; Zuo, X.; Yang, W.; Yousefzadeh, M.; Ramakrishana, S.; Li, H. High Performance Anti-Smog Window Screens via Electrospun Nanofibers. *J. Appl. Polym. Sci.* **2020**, *137*, 48657. [CrossRef]
31. Aydemir, H.; Demiryürek, O. The Effect of Electrospinning Parameters on Morphology and Diameter of Polyethylene Terephthalate (PET) and Recycled Polyethylene Terephthalate (r-PET) Nanofibers. *J. Text. Inst.* **2023**, *114*, 1443–1454. [CrossRef]
32. Bonfim, D.P.F.; Cruz, F.G.S.; Guerra, V.G.; Aguiar, M.L. Development of Filter Media by Electrospinning for Air Filtration of Nanoparticles from Pet Bottles. *Membranes* **2021**, *11*, 293. [CrossRef]
33. Bonfim, D.P.F.; Cruz, F.G.S.; Bretas, R.E.S.; Guerra, V.G.; Aguiar, M.L. A Sustainable Recycling Alternative: Electrospun Pet-Membranes for Air Nanofiltration. *Polymers* **2021**, *13*, 1166. [CrossRef]
34. Kijeńska-Gawrońska, E.; Wiercińska, K.; Werner, Ł.; Bil, M.; Staniszewska, M. From PET Bottle Waste to Antimicrobial Air Filters. *Macromol. Rapid Commun.* **2025**, *46*, 2400944. [CrossRef] [PubMed]
35. Hossain, M.T.; Shahid, M.A.; Ali, A. Development of Nanofibrous Membrane from Recycled Polyethene Terephthalate Bottle by Electrospinning. *OpenNano* **2022**, *8*, 100089. [CrossRef]

36. Medeiros, G.B.; de Souza, P.R.; Retamiro, K.M.; Nakamura, C.V.; Muniz, E.C.; Corradini, E. Experimental Design to Evaluate Properties of Electrospun Fibers of Zein/Poly (Ethylene Oxide) for Biomaterial Applications. *J. Appl. Polym. Sci.* **2021**, *138*, 50898. [CrossRef]
37. da Mata, G.C.; Morais, M.S.; de Oliveira, W.P.; Aguiar, M.L. Sustainable Surgical Masks: Optimizing Fine/Ultrafine Particle Filtration Using PVA/Chitosan Electrospun Nanofibers. *Environ. Sci. Nano* **2023**, *10*, 2185–2200. [CrossRef]
38. da Mata, G.C.; Morais, M.S.; Oliveira, W.P.; Aguiar, M.L. Spider-Net Structures in Electrospun Poly(Vinyl Alcohol)/Chitosan Nanofibers for Airborne Nanoparticle Filtration. *ACS Appl. Nano Mater.* **2025**, *8*, 11669–11681. [CrossRef]
39. Kim, H.B.; Lee, W.J.; Choi, S.C.; Lee, K.B.; Lee, M.-H. Filter Quality Factors of Fibrous Filters with Different Fiber Diameter. *Aerosol Sci. Technol.* **2020**, *55*, 154–166. [CrossRef]
40. Cai, R.-R.; Lu, H.; Zhang, L.-Z. Evaluation the Effect of Fiber Alignment on Particle Collection Performance of Mechanical/Electret Filters Based on Voronoi Tessellations. *Chem. Eng. Sci.* **2019**, *197*, 109–119. [CrossRef]
41. Subbiah, T.; Bhat, G.S.; Tock, R.W.; Parameswaran, S.; Ramkumar, S.S. Electrospinning of Nanofibers. *J. Appl. Polym. Sci.* **2005**, *96*, 557–569. [CrossRef]
42. Bortolassi, A.C.C.; Guerra, V.G.; Aguiar, M.L. Characterization and Evaluate the Efficiency of Different Filter Media in Removing Nanoparticles. *Sep. Purif. Technol.* **2017**, *175*, 79–86. [CrossRef]
43. De Barros, P.M.; Cirqueira, S.S.R.; Aguiar, M.L. Evaluation of the Deposition of Nanoparticles in Fibrous Filter. *Mater. Sci. Forum* **2014**, *802*, 174–179. [CrossRef]
44. Hinds, W.C. *Aerosol Technology: Properties, Behavior, and Measurement of Airborne Particles*, 2nd ed.; John Wiley & Sons: Hoboken, NJ, USA, 1998.
45. de Oliveira, A.E.; Aguiar, M.L.; Guerra, V.G. Improved Filter Media with PVA/Citric Acid/Triton X-100 Nanofibers for Filtration of Nanoparticles from Air. *Polym. Bull.* **2021**, *78*, 6387–6408. [CrossRef]
46. Domaschke, S.; Morel, A.; Kaufmann, R.; Hofmann, J.; Rossi, R.M.; Mazza, E.; Fortunato, G.; Ehret, A.E. Predicting the Macroscopic Response of Electrospun Membranes Based on Microstructure and Single Fibre Properties. *J. Mech. Behav. Biomed. Mater.* **2020**, *104*, 103634. [CrossRef] [PubMed]
47. Bellincanta, T.; Poletto, P.; Thürmer, M.B.; Duarte, J.; Toscan, A.; Zeni, M. Preparação e Caracterização de Membranas Poliméricas a Partir Da Blenda Polisulfona/Poliuretano. *Polímeros* **2011**, *21*, 229–232. [CrossRef]
48. Selatile, K.; Ray, S.S.; Ojijo, V.; Sadiku, R.E. Morphological, Thermal, and Mechanical Properties of Electrospun Recycled Poly(Ethylene Terephthalate)/Graphene Oxide Composite Nanofiber Membranes. *ACS Omega* **2021**, *6*, 21005–21015. [CrossRef]
49. Mahalingam, S.; Raimi-Abraham, B.T.; Craig, D.Q.M.; Edirisinghe, M. Solubility-Spinnability Map and Model for the Preparation of Fibres of Polyethylene (Terephthalate) Using Gyration and Pressure. *Chem. Eng. J.* **2015**, *280*, 344–353. [CrossRef]
50. Acevedo, F.; Hermosilla, J.; Sanhueza, C.; Mora-Lagos, B.; Fuentes, I.; Rubilar, M.; Concheiro, A.; Alvarez-Lorenzo, C. Gallic Acid Loaded PEO-Core/Zein-Shell Nanofibers for Chemopreventive Action on Gallbladder Cancer Cells. *Eur. J. Pharm. Sci.* **2018**, *119*, 49–61. [CrossRef]
51. Bhardwaj, N.; Kundu, S.C. Electrospinning: A Fascinating Fiber Fabrication Technique. *Biotechnol. Adv.* **2010**, *28*, 325–347. [CrossRef]
52. Keirouz, A.; Wang, Z.; Reddy, V.S.; Nagy, Z.K.; Vass, P.; Buzgo, M.; Ramakrishna, S.; Radacsi, N. The History of Electrospinning: Past, Present, and Future Developments. *Adv. Mater. Technol.* **2023**, *8*, 2201723. [CrossRef]
53. Kendouli, S.; Khalfallah, O.; Sobti, N.; Bensouissi, A.; Avci, A.; Eskizeybek, V.; Achour, S. Modification of Cellulose Acetate Nanofibers with PVP/Ag Addition. *Mater. Sci. Semicond. Process.* **2014**, *28*, 13–19. [CrossRef]
54. Clasen, C.; Eggers, J.; Fontelos, M.A.; Li, J.; McKinley, G.H. The Beads-on-String Structure of Viscoelastic Threads. *J. Fluid Mech.* **2006**, *556*, 283–308. [CrossRef]
55. Shenoy, S.L.; Bates, W.D.; Frisch, H.L.; Wnek, G.E. Role of Chain Entanglements on Fiber Formation during Electrospinning of Polymer Solutions: Good Solvent, Non-Specific Polymer-Polymer Interaction Limit. *Polymer* **2005**, *46*, 3372–3384. [CrossRef]
56. Abbas, J.A.; Said, I.A.; Mohamed, M.A.; Yasin, S.A.; Ali, Z.A.; Ahmed, I.H. Electrospinning of Polyethylene Terephthalate (PET) Nanofibers: Optimization Study Using Taguchi Design of Experiment. *IOP Conf. Ser. Mater. Sci. Eng.* **2018**, *454*, 012130. [CrossRef]
57. Kai, D.; Jin, G.; Prabhakaran, M.P.; Ramakrishna, S. Electrospun Synthetic and Natural Nanofibers for Regenerative Medicine and Stem Cells. *Biotechnol. J.* **2013**, *8*, 59–72. [CrossRef]
58. He, Z.; Rault, F.; Lewandowski, M.; Mohsenzadeh, E.; Salaün, F. Electrospun PVDF Nanofibers for Piezoelectric Applications: A Review of the Influence of Electrospinning Parameters on the β Phase and Crystallinity Enhancement. *Polymers* **2021**, *13*, 174. [CrossRef]
59. Nitti, P.; Gallo, N.; Natta, L.; Scalera, F.; Palazzo, B.; Sannino, A.; Gervaso, F. Influence of Nanofiber Orientation on Morphological and Mechanical Properties of Electrospun Chitosan Mats. *J. Healthc. Eng.* **2018**, *2018*, 3651480. [CrossRef]
60. Isaac, B.; Taylor, R.M.; Reifsnider, K. Mechanical and Dielectric Properties of Aligned Electrospun Fibers. *Fibers* **2021**, *9*, 4. [CrossRef]

61. Naeim, H.; Mahdavian, F.; Rodrigue, D. Journal of Environmental Chemical Engineering Review on Electrospinning of Recycled Polymer-Derived Fibers: A Road towards Sustainability, Production and Applications. *J. Environ. Chem. Eng.* **2025**, *13*, 119283. [CrossRef]
62. Al-abduljabbar, A.; Farooq, I. Electrospun Polymer Nanofibers: Processing, Properties, and Applications. *Polymers* **2023**, *15*, 65. [CrossRef]
63. Chinchillas-Chinchillas, M.J.; Orozco-Carmona, V.M.; Alvarado-Beltrán, C.G.; Almaral-Sánchez, J.L.; Sepulveda-Guzman, S.; Jasso-Ramos, L.E.; Castro-Beltrán, A. Synthesis of Recycled Poly(Ethylene Terephthalate)/Polyacrylonitrile/Styrene Composite Nanofibers by Electrospinning and Their Mechanical Properties Evaluation. *J. Polym. Environ.* **2019**, *27*, 659–669. [CrossRef]
64. Kijeńska-Gawrońska, E.; Wiercińska, K.; Bil, M. The Dependence of the Properties of Recycled PET Electrospun Mats on the Origin of the Material Used for Their Fabrication. *Polymers* **2022**, *14*, 2881. [CrossRef] [PubMed]
65. Celik, Y.; Shamsuyeva, M.; Endres, H.J. Thermal and Mechanical Properties of the Recycled and Virgin PET—Part I. *Polymers* **2022**, *14*, 1326. [CrossRef] [PubMed]
66. Little, H.A.; Tanikella, N.G.; Reich, M.J.; Fiedler, M.J.; Snabes, S.L.; Pearce, J.M. Towards Distributed Recycling with Additive Manufacturing of PET Flake Feedstocks. *Materials* **2020**, *13*, 4273. [CrossRef] [PubMed]
67. Kuzelova Kostakova, E.; Meszaros, L.; Maskova, G.; Blazkova, L.; Turcsan, T.; Lukas, D. Crystallinity of Electrospun and Centrifugal Spun Polycaprolactone Fibers: A Comparative Study. *J. Nanomater.* **2017**, *2017*, 8952390. [CrossRef]
68. Nayak, R.; Padhye, R. Nano Fibres by Electro Spinning: Properties and Applications. *J. Text. Eng. Fash. Technol.* **2017**, *2*, 486–497. [CrossRef]
69. Viora, L.; Combeau, M.; Pucci, M.F.; Perrin, D.; Liotier, P.-J.; Bouvard, J.-L.; Combeaud, C. A Comparative Study on Crystallisation for Virgin and Recycled Polyethylene Terephthalate (PET): Multiscale Effects on Physico-Mechanical Properties. *Polymers* **2023**, *15*, 4613. [CrossRef]
70. Park, H.-S.; Park, Y.O. Filtration Properties of Electrospun Ultrafine Fiber Webs. *Korean J. Chem. Eng.* **2005**, *22*, 165–172. [CrossRef]
71. Bortolassi, A.C.C.; Nagarajan, S.; de Araújo Lima, B.; Guerra, V.G.; Aguiar, M.L.; Huon, V.; Soussan, L.; Cornu, D.; Miele, P.; Bechelany, M. Efficient Nanoparticles Removal and Bactericidal Action of Electrospun Nanofibers Membranes for Air Filtration. *Mater. Sci. Eng. C* **2019**, *102*, 718–729. [CrossRef]
72. Abuzade, R.A.; Zadhoush, A.; Gharehaghaji, A.A. Air Permeability of Electrospun Polyacrylonitrile Nanoweb. *J. Appl. Polym. Sci.* **2012**, *126*, 232–243. [CrossRef]
73. Ng, W.L.; Zhou, L.; Sulong, A.B.; Ng, E.-P.; Tan, S.H. Modification of the Commercial Polyester Filter Media Support with Electrospun Polyethylene Terephthalate Fibers and Its Application for Air Purification. *Sci. Technol. Built Environ.* **2022**, *28*, 928–943. [CrossRef]
74. Bortolassi, A.C.C.; Guerra, V.G.; Aguiar, M.L. Evaluation of Different HEPA Filter Media for Removing Nickel Oxide Nanoparticles from Air Filtration. *Tecnol. Metal. Mater. Mineração* **2019**, *16*, 426–431. [CrossRef]
75. Lima, F.D.A.; Chagas, P.A.M.; Vieira, A.C.C.; Blanco, G.E.D.O.; Aguiar, M.L.; Guerra, V.G. Recycled PS and PET Hybrid Nanofiber Filter Media: Enhancing Mechanical Strength for Air Filtration. *J. Ind. Eng. Chem.* **2025**, *154*, 695–711. [CrossRef]
76. Shu, D.; Wang, L.; Liu, X.; Luo, S.; Zhang, Y.; Cheng, C.; Li, Z.; Jiao, L.; Yang, S.; Li, C.; et al. PET Nano-Woven Luminescent Fibers for Efficient Air Filtration and Fluorescence Indication of Particulate Matter. *Sep. Purif. Technol.* **2025**, *359*, 130401. [CrossRef]
77. Deng, L.; Zhang, P.; Zhang, W.; Zhu, R.; Yan, Y. High Filtration Efficiency Fluffy Material: Nano-Fiber Constructing Gradient Structure on Recycled Curved PET Micro-Fibers Web. *SN Appl. Sci.* **2019**, *1*, 190. [CrossRef]

Disclaimer/Publisher's Note: The statements, opinions and data contained in all publications are solely those of the individual author(s) and contributor(s) and not of MDPI and/or the editor(s). MDPI and/or the editor(s) disclaim responsibility for any injury to people or property resulting from any ideas, methods, instructions or products referred to in the content.